

# Polydisperse collision kernels in droplet-laden turbulence with implications for rain formation

Lukas A. Codispoti<sup>1,\*</sup>, Daniel W. Meyer<sup>1</sup>, and Patrick Jenny<sup>1</sup>

<sup>1</sup>Institute of Fluid Dynamics, ETH Zürich, Sonneggstrasse 3, 8092 Zürich, Switzerland

\*lukasco@ethz.ch

## ABSTRACT

We study the role of turbulence in enhancing the collisions of droplets within the cloud droplet bottleneck range. To this end, we perform direct numerical simulations of polydisperse inertial particles suspended in three-dimensional turbulence at high Reynolds number. Our analysis reveals that polydispersity enhances collisions of light droplets, but attenuates collisions at larger Stokes numbers by reducing the degree of inertial clustering and weakening the sling effect. We present a novel parameterization for the bidisperse collision kernel which blends the mechanisms related to inertial clustering and the sling effect with polydispersity. We then demonstrate that the droplet size distribution of typical cloud droplets is effectively broadened by turbulence and that droplet growth may be accelerated significantly by turbulent intermittency—a condition that the here provided theoretical contemplations in conjunction with recent measurements in clouds suggest is likely.

## Introduction

Cumulus clouds form in the shallow regions of earth’s atmosphere as warm, moist air rises and cools, upon which water vapor condenses at nucleation sites (solid aerosol particles) into tiny cloud droplets. Droplet growth is required in order for precipitation to occur. Initially, droplets grow by diffusion, until reaching radii of around  $r \approx 15\mu\text{m}$ , at which point diffusional growth becomes inefficient. Droplets also grow by gravitational settling, as large droplets fall faster and collide with smaller droplets, forming larger droplets through coalescence and, ultimately, falling to the ground in the form as rainfall. However, only droplets exceeding  $r > 40\mu\text{m}$  acquire sufficient settling velocity for gravitational collision-coalescence to become effective. In the range  $15\mu\text{m} < r < 40\mu\text{m}$ , neither diffusion nor gravitational settling provide adequate growth mechanisms—creating what is known as the condensation-coalescence *bottleneck* problem.<sup>1</sup> Despite this theoretical constraint, observations show warm convective clouds producing rain within 30 minutes. Turbulence, the non-linear chaotic motion of fluid flow, offers a compelling explanation for resolving this paradox. However, the role of air turbulence in broadening the droplet size distribution (DSD) is not well understood, and its incorporation in models of cloud microphysics remains lack-luster. Turbulence has been proposed to enhance droplet collisions within the bottleneck range through three key mechanisms: preferential concentration, polydispersity, and the sling effect.

Preferential concentration arises due to the interaction of inertial particles with turbulent vortices, leading to a non-uniform spatial distribution, also referred to as *clustering*. Particles tend to be expelled from regions of large vorticity and accumulate in strain-dominated areas, creating a compressible effective flow of particles.<sup>2</sup> The inertia of a particle is quantified by the Stokes number  $St = \tau_p / \tau_\eta$ , where  $\tau_p$  is the particle relaxation time and  $\tau_\eta$  is the Kolmogorov time, characterizing the timescale of the smallest turbulent eddies, also referred to as the *dissipative* scale. A particle with  $St \ll 1$  behaves like a fluid tracer, since its relaxation to the local conditions takes place quickly compared to how fast the flow fluctuates, whereas with  $St \gg 1$ , particles do not react to the flow easily and decorrelate from the carrier gas. In between the two extremes and most notably around  $St \approx 1$ , particles cluster (see, e.g., Refs. 3–5). Preferential concentration increases the collision rates between inertial particles by increasing the likelihood of particle encounters in regions of high number density.

Polydispersity, the presence of particles with varying sizes, introduces an additional collision-enhancing mechanism. Particles of different sizes interact differently with turbulent structures, leading to decorrelated trajectories and increased relative velocities between them. Also, differently-sized particles tend to cluster in different regions of the domain, meaning that inter-species preferential concentration is reduced. While this mechanism has been studied numerically in two-dimensional turbulence (e.g., Ref. 6) and three-dimensional turbulence at low Reynolds numbers (e.g., Refs. 7, 8), comprehensive three-dimensional analyses at high Reynolds numbers remain limited due to computational constraints. From a phenomenological standpoint, polydispersity merits investigation since cloud droplets are inherently size-distributed in nature. The present work addresses this data gap by providing a detailed investigation of polydisperse collision dynamics in high Reynolds number turbulence.

Finally, the sling effect<sup>9</sup> is the mechanism through which particles experience rare extreme turbulent events and are 'slung' out of vortices. This phenomenon occurs when particles from different flow regions cross trajectories, creating singularities in phase space, also known as caustics.<sup>10</sup> Caustic formation naturally leads to collisions between particles that travel on different branches of the phase-space manifold, i.e., exhibit different velocities while occupying the same location in physical space. The occurrence of caustics implies that inertial particles do not move on a continuum; thus, there is no well-defined Eulerian field that can describe the motion of the particles. The existence of caustics has been confirmed numerically<sup>11,12</sup> and experimentally.<sup>13</sup> Whether the sling effect is effective for the collision and coalescence of cloud droplets has been the subject of debate in recent years (see, e.g., Refs. 14–16). Many authors point out that typical cloud droplets exhibit Stokes numbers in the order of  $St \sim 10^{-2}$  to  $St \sim 10^{-1}$ , and are therefore too light to be susceptible to caustic formation. Others have argued that if cloud droplets with larger Stokes numbers exist, these also tend to have large settling parameters,  $Sv = \tau_p g / u_\eta$ , where  $g$  is the gravitational acceleration and  $u_\eta$  is the Kolmogorov velocity. Particles with  $Sv > 1$  settle faster under gravity than they interact with the dissipative scales of the turbulent flow, which means that inertial effects, including the sling effect, are negligible. However, recent measurements in convective clouds<sup>17,18</sup> reveal substantial local variations in the energy dissipation rate,  $\varepsilon$ . Turbulent flows are inherently intermittent: instead of being uniform, turbulent kinetic energy concentrates in localized, intense regions separated by relatively quiescent zones. Clouds exhibit very high Reynolds numbers  $Re_\lambda \sim 10^4$  (where  $Re_\lambda$  is the Taylor-scale Reynolds number), implying that fluctuations of the local dissipation rate are significant. Since  $St \propto r^2 \varepsilon^{1/2}$  and  $Sv \propto r^2 \varepsilon^{-1/4}$ , it is likely that a fraction of droplets in a warm cloud experiences short-lived turbulent conditions conducive to caustic formation, even when average conditions would suggest otherwise. Recent reports<sup>19,20</sup> of strongly heterogeneous droplet populations in atmospheric clouds further support this claim. A small fraction of large droplets may be enough to 'seed' a cloud and create a run-away effect, i.e., to create large enough droplets that subsequently collide with smaller droplets under gravitational settling, or, as we will show in the present work, due to purely inertial effects in the absence of gravity.

It is of particular interest for the atmospheric physics community to develop models that accurately capture the relevant physical conditions occurring on the length scale of cloud droplets, often referred to as microphysics schemes. State-of-the-art numerical simulations of cumulus clouds involve large-eddy simulations (LESs) which only resolve the largest scales of the turbulent flow in conjunction with the super-droplet method.<sup>21</sup> In these models, collision kernels are used to calculate the transfer of mass from smaller to larger droplets. These kernels are typically parameterized based on droplet properties and the local thermodynamic and flow conditions. For example, two recent studies<sup>22,23</sup> used this approach to simulate rain formation in a convective cloud, demonstrating that turbulence significantly enhances the broadening of the droplet size distribution (DSD). The effect of turbulence was incorporated through the celebrated collision kernel of Ayala et al.<sup>24</sup>, which, by construction, is only valid for droplets with  $Sv > 1$ . However, cloud droplets in the bottleneck range typically exhibit sub-unity settling parameters, motivating new developments in the field.

In this study, we perform an extensive DNS campaign of fully-resolved, three-dimensional particle-laden turbulence at  $Re_\lambda = 418$ . Our aim is to study the roles of the collision mechanisms that are possibly involved in the collision-coalescence bottleneck problem. In particular, we provide a map of collision kernels between bidisperse particle pairs as a function of their Stokes numbers, which, to the best of our knowledge, is the first of its kind for high Reynolds number turbulence. In addition, we consider the hypothesis that turbulent intermittency accelerates cloud droplet growth and perform numerical simulations that support this claim.

## Results

Inertial particles suspended in three-dimensional homogeneous isotropic turbulent flows are considered. The flow velocity field  $\mathbf{u}(\mathbf{x}, t)$  is the solution of the incompressible Navier-Stokes equation. We neglect gravity, implying that  $Sv \ll 1$ . Furthermore, we assume that particles are small ( $r \ll \eta$ , where  $\eta$  is the Kolmogorov length scale) and heavy compared to the carrier gas ( $\rho_p / \rho_f = 800$ ). Under these conditions, particles neither disturb the flow nor experience significant hydrodynamic interactions, allowing their motion to be described by the point-particle approximation<sup>25</sup>

$$\dot{\mathbf{x}} = \mathbf{v}, \quad \dot{\mathbf{v}} = \frac{\mathbf{u}(\mathbf{x}, t) - \mathbf{v}}{\tau_p}. \quad (1)$$

Here,  $\mathbf{x}(t)$  and  $\mathbf{v}(\mathbf{x}(t), t)$  are the Lagrangian particle position and velocity, respectively. The point-particle approach is justified for atmospheric clouds, where typical droplet volume fractions are of the order of<sup>1</sup>  $\Phi_p = V_p / V \sim 10^{-6}$ . Throughout this work, we will use the terms 'particle' and 'droplet' interchangeably.

Collision statistics are computed using the ghost-collision approach, where particles pass through each other without interaction. The collision rate  $\mathbb{N}_{ij}$  between particles of species  $i$  and  $j$  is determined by counting the number of pairs per unit time satisfying the contact condition  $|\Delta \mathbf{x}| < R = r_i + r_j$ , where  $\Delta \mathbf{x} = \mathbf{x}_i - \mathbf{x}_j$  denotes the relative position vector and  $r_i$  and  $r_j$  are the radii of the particles, respectively. The dynamic collision kernel  $\Gamma_{ij} = \mathbb{N}_{ij} / (n_i n_j)$  is thence obtained by normalizing

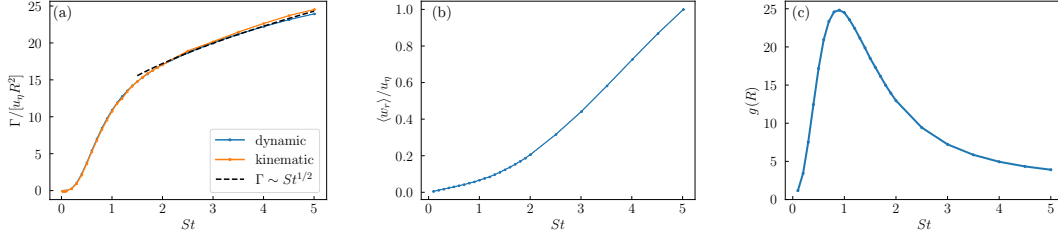


**Figure 1.** Monodisperse (a) collision kernel, (b) RRV and (c) RDF at contact as a function of the Stokes number.

with the respective number densities,  $n_i$  and  $n_j$  (in the monodisperse case  $i = j$ , the kernel is multiplied by a 2). A kinematic formulation of the collision kernel was derived by Sundaram & Collins<sup>26</sup> as

$$\Gamma^{(\text{kin})} = 2\pi R^2 \langle w_r \rangle g(R). \quad (2)$$

Here,  $w_r = \frac{|\Delta \mathbf{v} \cdot \Delta \mathbf{x}|}{|\Delta \mathbf{x}|} \Big|_{r=R}$  is the Radial Relative Velocity (RRV) at contact, where  $r = |\Delta \mathbf{x}|$  and  $\Delta \mathbf{v} = \mathbf{v}_i - \mathbf{v}_j$ . The term  $g(R)$  is the Radial Distribution Function (RDF) at contact, quantifying the degree of preferential concentration. The bidisperse RDF is symmetric ( $g_{ij}(r) = g_{ji}(r)$ ) and computes as

$$g_{ij}(r) = \frac{\langle N_j \rangle_i(r) / V_{\text{shell}}}{N_{ij} V}, \quad (3)$$

where  $\langle N_j \rangle_i(r)$  is the average number of particles of species  $j$  separated from a particle  $i$  by a distance within the spherical shell of volume  $V_{\text{shell}} = 4\pi((r + \delta/2)^3 - (r - \delta/2)^3)/3$ ,  $N_{ij}$  is the number of  $(i, j)$  particle pairs, and  $V$  is the total system volume. Essentially, Eq. (2) states that the combined effects of preferential concentration and the sling effect can be represented by the product  $\langle w_r \rangle g(R)$ . Unlike the dynamic collision kernel, which is computed by directly counting the number of collisions, Eq. (2) represents a kinematic formulation, but is valid only for suitable calculation of the unclosed terms  $\langle w_r \rangle$  and  $g(R)$ , which does not offer any computational advantages compared to the dynamic kernel.

### Monodisperse suspensions

Results for the monodisperse case are presented in Fig. 1. In panel (a), the dynamic and kinematic collision kernels, scaled by the characteristic collision volume swept per unit time by a flow tracer,  $R^2 u_\eta$ , are plotted against the Stokes number. It is worth recalling that both are direct measurements of the collision kernel. Therefore, the kinematic recovers the dynamic collision kernel within statistical uncertainty, which Fig. 1(a) confirms in the affirmative. We have verified that this also holds true for the bidisperse suspensions (not shown).

The collision kernel increases rapidly with the Stokes number, most notably in the range from  $St \approx 0.3$  to  $St \approx 1$ . The dependence of the collision kernel on the Stokes number can be understood by examining the two terms appearing in Eq. (2): the RRV and the RDF at contact, shown in Figs. 1(b) and (c), respectively. The growth of  $\langle w_r \rangle$  is gentle and approximately linear at first, but increases more rapidly at larger  $St$ . This behavior is attributed to the sling effect, which becomes increasingly important as the Stokes number increases. The RDF (Fig. 1(c)), on the other hand, is notably non-monotonic. Particles disperse homogeneously in space with  $St \rightarrow 0$  and  $St \rightarrow \infty$ , respectively, resulting in  $g(R) = 1$  in both limits. In between, the RDF peaks at  $St \approx 1$ , commonly known to be the Stokes number with maximum clustering. The dependence of  $\Gamma$  on the Stokes number can thence be interpreted as the combined effect of  $\langle w_r \rangle$  and  $g(R)$ . It is tempting to attribute the steep increase of the collision kernel between  $St \approx 0.3$  and  $St \approx 1$  to preferential concentration, since the RDF grows at a slope far greater than that of the RRV. However, separating preferential concentration and the sling effect in this manner is not possible, since caustics are also involved in facilitating clustering.<sup>27</sup> In an elegant study, Vosskuhle et al.<sup>28</sup> showed that the sling effect already significantly contributes to the collision dynamics at  $St \gtrsim 0.75$ , yet the ensemble-averaged RRV only weakly affects the product  $\langle w_r \rangle g(R)$  in this range, as shown in Fig. 1(b).

While preferential concentration decreases with Stokes numbers exceeding  $St = 1$ , the RRV continues to grow at an increasing rate. Beyond  $St \gtrsim 2$ , our data suggests a scaling of the collision kernel proportional to  $St^{1/2}$ , as indicated by the dashed line in Fig. 1(a). This scaling is consistent with theoretical predictions<sup>29,30</sup> of the RRV in the sling-dominated regime at high Reynolds numbers, where the motion of the individual particles becomes increasingly uncorrelated with the underlying flow field. In this regime, particle velocities are randomly distributed, making a gas-kinetic approach following Abrahamson<sup>31</sup> more appropriate. It has been suggested that the collision kernel should be expressed as the sum  $\Gamma = \Gamma_{\text{adv}} + \Gamma_{\text{sling}}$ , explicitly differentiating between the collision of particles that experience caustics and those that do not.<sup>28,29</sup>

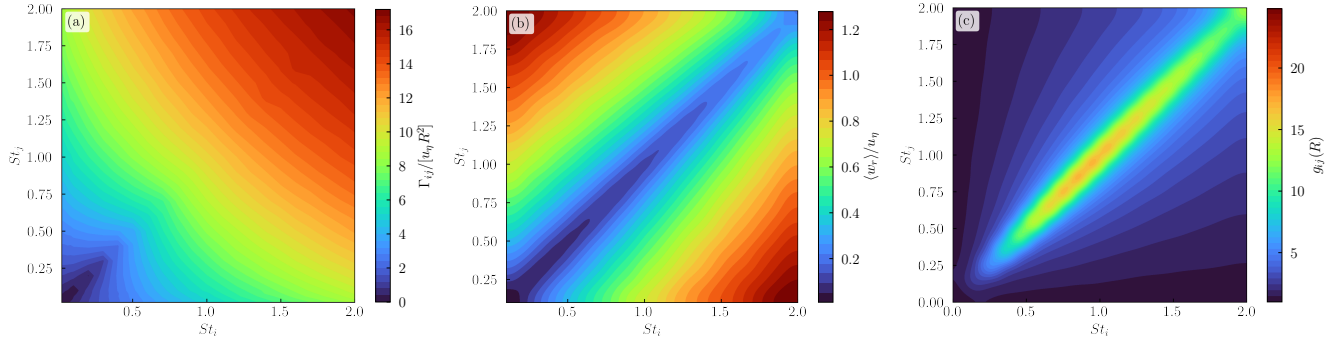


**Figure 2.** Bidisperse (a) collision kernel, (b) RRV and (c) RDF at contact.

The data shown in Fig. 1 is in good agreement with previous numerical studies (e.g., Refs. 28, 32, 33). The monodisperse collision kernel has been found to remain largely insensitive to changes in  $Re_\lambda$ , justifying the examination of droplet collisions in numerical simulations at Reynolds numbers that are computationally feasible yet lower than those occurring in atmospheric clouds.

### Bidisperse suspensions

Now, how does polydispersity, naturally occurring in cloud droplet populations, affect the collision dynamics? To address this question, we compute the collision kernel, RRV and RDF at contact for particle pairs  $(i, j)$  with Stokes numbers ranging from  $St = 0.02$  to  $St = 2$ , as shown in Fig. 2.

It is readily verified that all matrices are symmetric. In agreement with the monodisperse results, the collision rate generally increases with the Stokes number, resulting from the combined effects of  $\langle w_r \rangle$  and  $g(R)$ . We observe that the RRV increases with the separation of the Stokes numbers of the colliding pair, i.e.,  $\langle w_r \rangle_{ij} \geq \langle w_r \rangle_{ii}$  and  $\langle w_r \rangle_{ij} \geq \langle w_r \rangle_{jj}$ . The enhancement of the RRV due to differential sampling is largely outweighing its increase along the diagonal, i.e., for the monodisperse case (Fig. 1(b)). The RDF behaves in the opposite manner:  $g(R)$  is maximal around the diagonal, and quickly drops as the Stokes numbers separate. This indicates that preferential concentration is strongly attenuated by differential sampling.

We observe that the behavior of the bidisperse collision kernel falls into two regimes, depending on the Stokes numbers of the colliding pair. At small Stokes numbers (i.e., when both  $St_i, St_j \lesssim 0.5$ ), polydispersity enhances the collision kernel even if it involves reducing the Stokes number of one of the colliding droplets. This can be observed in Fig. 2(a): starting from a point on the diagonal (with  $St_i, St_j \leq 0.5$ ), moving horizontally or vertically towards a smaller Stokes number for one particle (while the other remains fixed) leads to an increase in  $\Gamma$ . To explain this behavior, consider the competing effects of polydispersity to decrease particle clustering yet increase relative motion. At small Stokes numbers, particles tend not to detach from the flow, and preferential concentration is weak. As a result, the enhancement of the relative velocities due to differential sampling is more significant, and the net effect of polydispersity on the collision kernel is positive.

Conversely, in the regime where the Stokes numbers of both particles exceed  $St \gtrsim 0.5$ , polydispersity attenuates collisions, because the reduction in preferential concentration dominates the increase in the relative velocities. In this case, the collision kernel only increases when moving horizontally to the right or vertically upwards in Fig. 2(a), i.e., when the Stokes number of one particle grows. To elucidate this point further, consider Fig. 3, which shows the bidisperse collision kernel as a function of the mean Stokes number  $\langle St \rangle = (St_i + St_j)/2$  and the dispersion parameter  $\theta_{ij} = |St_i - St_j|/(St_i + St_j)$ . It is evident that  $\Gamma_{ij}$  predominantly increases with  $\langle St \rangle$ , as indicated by the nearly vertical contour lines. The dependence on  $\theta_{ij}$  is secondary and limited to the smallest values of  $\langle St \rangle$ . This suggests that as the particles' inertia increases, the specific size difference becomes less critical than the overall inertial effects of preferential concentration and the sling effect. For large  $\langle St \rangle$ , increasing  $\theta_{ij}$  (at constant  $\langle St \rangle$ ) even decreases  $\Gamma_{ij}$ , as greater differences in size weakens preferential concentration.

James & Ray<sup>6</sup> have reported bidisperse collision kernels obtained from DNS of two-dimensional particle-laden turbulence. Their data show a significant increase of the collision rate along the diagonal, implying that collisions of same-sized particles are strongly enhanced. Our data (Fig. 2(a)) does not exhibit this behavior. In preparing this paper, we found that this discrepancy is possibly related to the algorithm used to detect ghost collisions, as explained in the Methods section below. More fundamentally, cloud droplet dynamics are inherently three-dimensional processes. The distinct characteristics of 2D turbulence, such as the inverse energy cascade, may not accurately capture the collision dynamics relevant to cloud droplets. Two-dimensional turbulence lacks the flow structures and intermittency associated with three-dimensional turbulence, which are possibly crucial for the collision dynamics of cloud droplets. For example, it has been demonstrated<sup>11,12</sup> that caustic formation occurs through specific flow topologies unique to 3D turbulence.

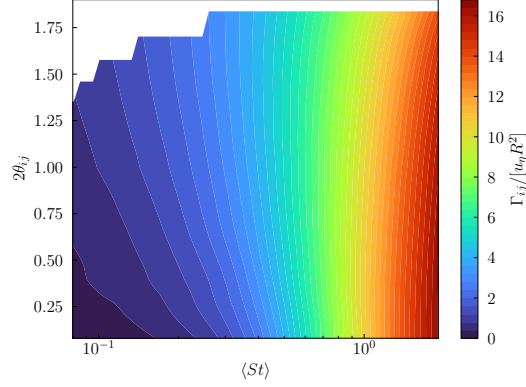


**Figure 3.** Bidisperse collision kernel as a function of the mean Stokes number  $\langle St \rangle$  (logarithmic scale) and the dispersion parameter.

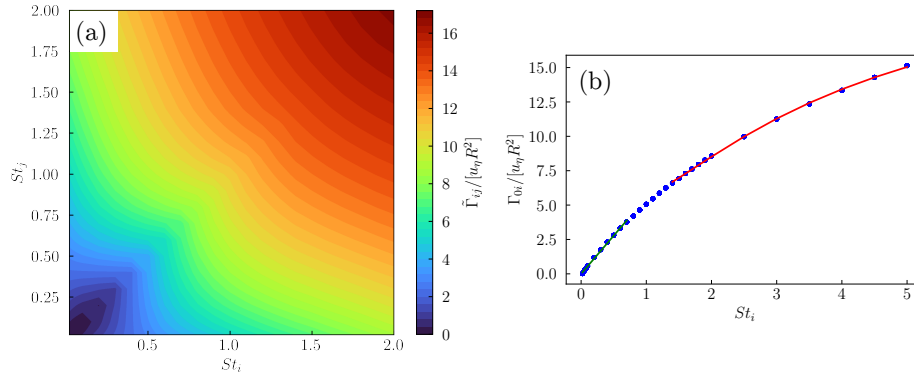


**Figure 4.** (a) Parameterization of the bidisperse collision kernel and (b) the component  $\Gamma_{0i}$  obtained from the DNS with  $St_0 = 0.02$ . In panel (b), the dots depict the DNS data and the green and red lines show  $\Gamma \sim St_i$  and  $\Gamma \sim \exp(-1/St_i)$  data fits, respectively.

### Parameterization

We find that the bidisperse collision kernel for a droplet pair  $(i, j)$  with  $St_i \leq St_j$  can be effectively parameterized as

$$\tilde{\Gamma}_{ij} = \tilde{\Gamma}(St_i, St_j) = \theta_{ij}\Gamma_{0i} + (1 - \theta_{ij})\Gamma_{ii}. \quad (4)$$

Here,  $\Gamma_{ii}$  is the monodisperse collision kernel for particles with Stokes number  $St_i$  (as shown in Fig. 1), and  $\Gamma_{0i}$  is the collision kernel between particles of  $St_i$  and very light, practically tracer particles (shown in Fig. 4(b) with  $St_0 = 0.02$ ). Expression (4) blends the contributions associated with inertial clustering and the sling effect (hereafter referred to as 'inertial effects'), represented by the monodisperse kernel  $\Gamma_{ii}$ , with those associated with polydispersity, i.e., differential sampling (represented by  $\Gamma_{0i}$ ). The weighting is determined by the dispersion parameter  $\theta_{ij} = |St_i - St_j|/(St_i + St_j)$ . One easily verifies that as  $St_j \rightarrow 0$ , the correct asymptotic behavior  $\tilde{\Gamma}_{ij} = \Gamma_{0i}$  is recovered. Similarly, for  $i = j$ , Eq. (4) simplifies to the monodisperse collision kernel.

The validity of Eq. (4) as a parameterization for the bidisperse collision kernel is demonstrated in Fig. 4(a). The values obtained from the parameterization agree remarkably well with the DNS data (Fig. 2(a)). The model accurately captures the enhancing effect of polydispersity at small Stokes numbers, even if the mean Stokes number of the colliding pair is reduced. This is because initially,  $\Gamma_{0i}$  (Fig. 3(b)) increases more rapidly with  $St_i$  through differential sampling than  $\Gamma_{ii}$  increases through inertial effects. Conversely, at larger Stokes numbers, polydispersity attenuates collisions, since  $\Gamma_{ii} > \Gamma_{0i}$  for  $St_i > 0.5$ .

To obtain Fig. 4(a),  $\tilde{\Gamma}$  was evaluated with the kernels  $\Gamma_{0i}$  and  $\Gamma_{ii}$  obtained from the DNS data. In general, these terms are unclosed. Modeling the bidisperse turbulent collision kernel therefore leaves one with the task of developing models for  $\Gamma_{0i}$  and  $\Gamma_{ii}$ . As described above, the monodisperse kernel is affected by the combined mechanisms of preferential concentration and the sling effect. Modeling it remains an active area of research, which is beyond the scope of the present work. Most models exploit that the collision kernel can be expressed by the product of the terms  $\langle w_r \rangle$  and  $g(R)$ , which appear to follow

power-law behaviors<sup>33</sup> and/or rely on fitting to DNS data (e.g., Ref. 34). A fundamental difficulty for the modelling of the monodisperse collision rate is the fact that  $w_r$  depends largely on the 'memory' that particles collect along different trajectories before collisions occur.<sup>30</sup>

In comparison, modeling the  $\Gamma_{0r}$  kernel is more straightforward. In this case, preferential concentration does not play a role, and the collision dynamics reduce to the effect of the RRV. James & Ray<sup>6</sup> have derived analytical expressions for  $w_r$  based on assumptions that apply to different scenarios. They demonstrate that with  $St_j \ll 1$ , the RRV obeys the linear scaling  $w_r \sim St_i$  if  $St_i \lesssim 1$  and exponential scaling of the form  $w_r \sim \exp(-1/St_i)$  for  $St_i \gg 1$ . Since  $g(R) \approx 1$  in this regime, we can apply the scaling of the RVV to that of the collision kernel. In Fig. 4(b), we show the  $\Gamma_{0r}$  kernel obtained by approximating  $St_0 = 0.02$  and apply the two scaling laws. It is evident that the kernel agrees well with the predictions for  $w_r$  provided by Ref. 6.

### Simulations with coalescence

We now move away from the ghost collision approach and turn to simulations in which colliding pairs merge into single droplets, with collision efficiency of one. Our goal here is to illustrate how intermittency in turbulence, manifested by irregular fluctuations of the local energy dissipation rate, affects the broadening of the droplet size distribution (DSD) in atmospheric clouds. While one could simulate the effect of intermittency by increasing the Reynolds number, this approach rapidly becomes computationally prohibitive. Instead, we emulate the effect of increasing the dissipation rate by exploiting that the Stokes number scales as  $St \sim r^2 \varepsilon^{1/2}$ . Thus, increasing the dissipation rate by a factor  $\alpha^4$  is equivalent to increasing the droplet size by  $\alpha$  while keeping the flow field unchanged. This equivalence allows us to simulate the effect of increased intermittency by scaling the initial DSD rather than performing computationally expensive DNS at higher Reynolds numbers. To keep the droplet volume fraction  $\Phi_p \propto nr^3$  unchanged, the number of droplets is reduced accordingly by a factor of  $\alpha^{-3}$ . A cloud-realistic value of  $\Phi_p = 8.5 \cdot 10^{-6}$  is used.

Droplet populations are initialized with radii following a Gaussian distribution,  $r \sim \mathcal{N}(r_0, \sigma_r^2)$ , with mean  $r_0$  and standard deviation  $\sigma_r$ , as is expected to result from condensation. Both  $r_0$  and  $\sigma_r$  are then scaled by  $\alpha$ , so that a shift in the local energy dissipation rate by a factor of  $\varepsilon/\varepsilon_0 = \alpha^4$  is emulated. For example, by setting  $\alpha = 1.75$ , we adjust the mean Stokes number from  $\langle St \rangle = 0.23$  to  $\langle St \rangle = 0.69$ , corresponding to a 9.38-fold increase in the local energy dissipation rate, which is well within measurements in atmospheric clouds.<sup>17</sup> The remaining cases are tabulated in Table 1.

$\alpha$	$\langle St \rangle$	$\varepsilon/\varepsilon_0$
1	0.23	1
1.33	0.4	3.13
1.75	0.69	9.38
2.1	1	19.45

**Table 1.** Scaling factor  $\alpha$ , mean Stokes number and corresponding increase in the local dissipation rate.

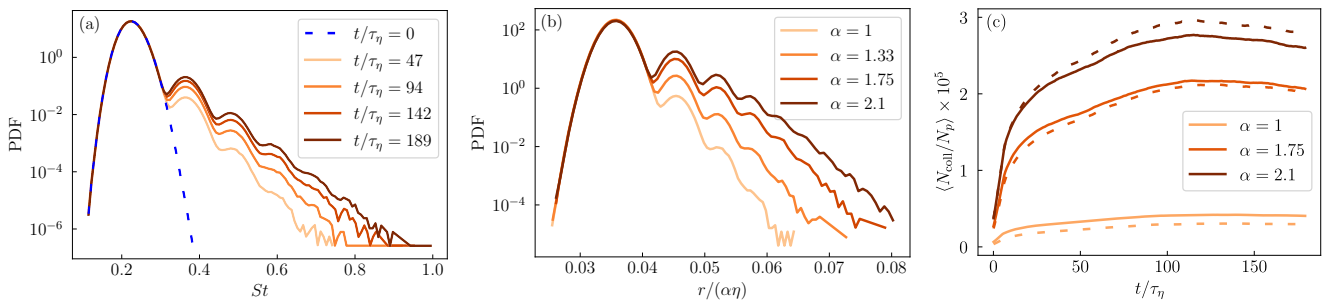


**Figure 5.** Results for the DNS with coalescing droplets. (a) Evolution of the DSD given by the probability distribution function of the droplet Stokes number obtained from the base case ( $\alpha = 1$ ). The initial distribution is shown by the dashed blue curve. (b) DSD in terms of the scaled droplet radius after  $t = 189\tau_p$  for different values of  $\alpha$ . (c) Evolution of the time-averaged rate of collision-coalescence (solid lines) for different values of  $\alpha$ , along with monodisperse reference simulations (dashed lines).

The base case ( $\alpha = 1$ ) exhibits a mean Stokes number of  $\langle St \rangle = 0.23$ , and mean radius  $r_0 = 0.036\eta$ . Assuming that in an atmospheric cloud, the Kolmogorov length scale is<sup>17</sup>  $\eta \approx 0.4\text{mm}$ , the base case is representative of droplets at the lower end of the bottleneck range ( $r_0 \approx 14\mu\text{m}$ ). The broadening of the DSD in the base case is illustrated in Fig. 5(a). The droplet size

is given in terms of the Stokes number, and the curves shown represent the probability density function (PDF), evaluated at equidistant bins. It is evident that the DSD broadens rapidly from its initial narrow Gaussian distribution (shown by the dashed blue curve), with large droplets appearing after short times. This indicates that turbulence by itself is effective in promoting droplet growth even for small, typical cloud droplets. The distributions develop long tails with 'bumpy' profiles, owing to the narrow initial distributions and the binary nature of coalescence events. It is worth noting that the Kolmogorov time in an atmospheric cloud is of the order of  $\tau_\eta \sim 0.01$ s, meaning that the DSD depicted in Fig. 5(a) evolves within very short time intervals. The DSD continues to broaden, even though we do not supply the system with new liquid water. After  $t = 189\tau_\eta$ , the largest droplets have  $St \approx 1$ , corresponding to a droplet radius of  $r \approx 30\mu\text{m}$ .

Figure 5(b) depicts DSDs for different values of  $\alpha$  after an integration time of  $t = 189\tau_p$ . In reality, an increase in the local dissipation rate would increase the Stokes number of a cloud droplet by decreasing  $\tau_\eta$ . In our study, however, the flow field remains unchanged, whereas the droplet phase is altered. For a meaningful comparison of the DSDs across different values of  $\alpha$ , we therefore fixed the instance in time in terms of  $\tau_p$  instead of the flow timescale. The curves in Figure 5(b) represent the PDFs of the droplet radii scaled back by the factor  $\alpha$ . This means that the horizontal axis depicts the radii of the droplets under the conditions of the base case, approximately spanning the bottleneck range (again, assuming  $\eta \approx 0.4\text{mm}$ ). We observe that the droplet growth significantly accelerates with increasing  $\alpha$ . The fraction of droplets that overcome the size gap clearly grows with  $\alpha$ , indicating that the local turbulence intensity effectively promotes droplet growth. The largest differences are observed between the cases with  $\alpha = 1$ ,  $\alpha = 1.33$  and  $\alpha = 1.75$ , exhibiting increases in the mean Stokes number from  $\langle St \rangle = 0.23$  to  $\langle St \rangle = 0.4$  and  $\langle St \rangle = 0.69$ , respectively. Here, the effect is most pronounced, consistent with our findings above that the largest increases of the collision kernel occur within this Stokes number range (Fig. 1(a)).

Figure 5(c) shows the time-averaged fraction of droplets that undergo collision and coalescence as it evolves in time. All cases show statistical stationarity after around  $t = 100\tau_\eta$ . The collision rate strongly increases with  $\alpha$ : compared to the base case, the collisions occur around 5.3 and 7 times more frequently with  $\alpha = 1.75$  and  $\alpha = 2.1$ , respectively. This data supports the theory that short-lived intense turbulent events may significantly accelerate droplet growth. In addition, Figure 5(c) displays the collision-coalescence rates for monodisperse reference simulations (dashed lines). In the base case, the collision rate is around 50% higher compared to the monodisperse suspension initialized with the matching mean Stokes number, indicating that polydispersity effectively enhances droplet growth. For the case with  $\alpha = 1.75$ , on the other hand, the polydisperse enhancement reduces to merely 5%, and for  $\alpha = 2.1$ , the monodisperse collision rate is higher by around 5%. This reflects our findings above that polydispersity enhances collisions at small Stokes numbers, but attenuates them at larger Stokes numbers. Depending on the local turbulence intensity, narrow DSDs in atmospheric clouds can therefore broaden faster than wide DSDs.

## Discussion

We have studied turbulent droplet collisions at high Reynolds numbers by means of direct numerical simulations (DNSs) to investigate the interplay of preferential concentration, the sling effect and polydispersity in the collision dynamics of cloud droplets. The bidisperse collision kernel for a wide range of Stokes numbers has been obtained. This data is important in understanding how turbulence affects cloud droplet growth. The simulations were performed in the absence of gravity, to address specifically the cloud droplet bottleneck range, in which droplets are too large to grow by diffusion but too light to collide under gravitational settling.

Our findings establish that polydispersity is an effective mechanism by which droplets collide under turbulence, even in the absence of gravity. This contrasts with the conventional view that primarily links polydispersity to collisions induced by gravitational settling. Our data suggest that differential sampling of the turbulent flow by differently-sized droplets is a significant contributor to droplet collisions, a mechanism that has been largely overlooked in cloud microphysics models.

The influence of polydispersity is highly dependent on the Stokes number. At small Stokes numbers ( $St \lesssim 0.5$ ), polydispersity enhances collisions because the increased relative velocities from differential sampling dominate over the weak preferential concentration. Conversely, at larger Stokes numbers, polydispersity attenuates collisions because it weakens both preferential concentration and the sling effect, which are the dominant mechanisms at higher inertia and strongly increase the collision rate in this regime. Thus, the role of polydispersity transitions from being a facilitator to a suppressor of collisions as particle inertia increases.

A key contribution of this work is the introduction of a novel, physically transparent parameterization for the bidisperse turbulent collision kernel. By blending monodisperse inertial effects with polydispersity-driven differential sampling, our model captures the essential physics across the relevant Stokes number regimes. This parameterization reduces the complexity of the bidisperse kernel to two one-dimensional measurements and may serve as a foundation for the development of more general models for the turbulent collision kernel in cloud microphysics schemes.

Through simulations of coalescing droplets, we have shown that turbulence alone can bridge the size gap. Rapid broadening of the droplet size distribution (DSD) due to turbulence was observed even for typical cloud droplets with Stokes numbers around  $St \approx 0.2$ , providing a viable pathway for growth within the bottleneck range.

It has been postulated that turbulent intermittency in clouds may play a crucial role in overcoming the bottleneck problem. Our simulations provide evidence supporting this hypothesis. By simulating an increase in the local energy dissipation rate, we observed a dramatic enhancement in droplet growth rates. This suggests that short-lived, intense turbulent events within clouds could be a key factor in accelerating the onset of precipitation. Depending on the Stokes number regime (or the local turbulence intensity, respectively), initially narrow droplet size distributions can broaden faster than wider ones. This highlights the complex, non-trivial relationship between the initial droplet population and its subsequent evolution in a turbulent environment, warranting further investigation.

Looking ahead, we plan to incorporate our findings into the microphysics scheme of large-eddy simulations (LESs) of convective clouds. This will allow for a more accurate representation of polydispersity, which is often neglected in current models. Through this, we will further investigate the role of turbulent intermittency in a more realistic, large-scale atmospheric context to better quantify its impact on droplet growth and rain formation.

## Methods

We utilize flow fields of forced isotropic homogeneous turbulence obtained from the Johns Hopkins Turbulence Database.<sup>35</sup> These fields are generated by solving the incompressible Navier-Stokes equations using a pseudo-spectral method. The computational domain consists of a periodic cube of length  $L = 2\pi$ , discretized into  $N_g = 1024^3$  grid points. The Taylor-scale Reynolds number is  $Re_\lambda = 418$ , while the Kolmogorov length and time scales are  $\eta = 0.0028$  and  $\tau_\eta = 0.0424$ , respectively. Equation (1) is solved for large ensembles of particles by trilinearly interpolating the flow velocity to the particle positions and using an exponential integration scheme. Particles are treated as points. Each particle is assigned a mass  $m$ , which implies its radius  $r = (3m/(4\pi\rho_p))^{1/3}$  and relaxation time  $\tau_p = 2r^2\rho_p/(9\nu\rho_f)$ . For a more detailed description of the simulation setup we refer to our previous publication.<sup>12</sup>

The particles are initialized uniformly at random in the domain with the local flow velocity. A precursor simulation is performed for a time  $t_0 = 165\tau_\eta$  to ensure statistical stationarity of the collision rate. The simulations are then restarted from  $t_0$  and the ghost collision algorithm is used to detect collisions. To avoid overestimation of the collision rate in case of strong preferential concentration (specifically for monodisperse suspensions), the first ten time steps are discarded to reject collisions that occurred at times  $t < t_0$  and those that are recorded over multiple time steps. Each particle pair is only allowed to collide once. Particle trajectories are linearly extrapolated to detect between-time step collisions. For the simulations with coalescence, each colliding particle pair  $(i, j)$  is removed and replaced by a new particle introduced at the position  $\mathbf{x}_{\text{new}} = (m_i\mathbf{x}_i + m_j\mathbf{x}_j)/(m_i + m_j)$  with mass  $m_{\text{new}} = m_i + m_j$  and velocity  $\mathbf{v}_{\text{new}} = (m_i\mathbf{v}_i + m_j\mathbf{v}_j)/(m_i + m_j)$ .

## Acknowledgements

This research was supported by funding from the Swiss National Science Foundation (grant 204621). Numerical simulations were carried out using the resources provided by the *Euler* cluster of ETH Zürich.<sup>36</sup>

## Author contributions statement

L.A.C. performed the simulations. All authors analyzed the results. D.W.M. lead the acquisition of funding. P.J. supervised the project. L.A.C. wrote the original manuscript. All authors reviewed the manuscript.

## Additional information

The authors declare no competing interests.

## References

1. Grabowski, W. W. & Wang, L.-P. Growth of Cloud Droplets in a Turbulent Environment. *Annu. Rev. Fluid Mech.* **45**, 293–324, DOI: [10.1146/annurev-fluid-011212-140750](https://doi.org/10.1146/annurev-fluid-011212-140750) (2013).
2. Maxey, M. R. The gravitational settling of aerosol particles in homogeneous turbulence and random flow fields. *J. Fluid Mech.* **174**, 441–465, DOI: [10.1017/S0022112087000193](https://doi.org/10.1017/S0022112087000193) (1987).
3. Squires, K. D. & Eaton, J. K. Preferential concentration of particles by turbulence. *Phys. Fluids A: Fluid Dyn.* **3**, 1169–1178, DOI: [10.1063/1.858045](https://doi.org/10.1063/1.858045) (1991).
4. Cencini, M. *et al.* Dynamics and statistics of heavy particles in turbulent flows. *J. Turbul.* **7**, N36, DOI: [10.1080/14685240600675727](https://doi.org/10.1080/14685240600675727) (2006).

5. Ray, B. & Collins, L. R. Preferential concentration and relative velocity statistics of inertial particles in Navier–Stokes turbulence with and without filtering. *J. Fluid Mech.* **680**, 488–510, DOI: [10.1017/jfm.2011.174](https://doi.org/10.1017/jfm.2011.174) (2011).
6. James, M. & Ray, S. S. Enhanced droplet collision rates and impact velocities in turbulent flows: The effect of polydispersity and transient phases. *Sci. Reports* **7**, 12231, DOI: [10.1038/s41598-017-12093-0](https://doi.org/10.1038/s41598-017-12093-0) (2017).
7. Nair, V., Devenish, B. & van Reeuwijk, M. Effect of Gravity on Particle Clustering and Collisions in Decaying Turbulence. *Flow, Turbul. Combust.* **110**, 889–915, DOI: [10.1007/s10494-023-00402-9](https://doi.org/10.1007/s10494-023-00402-9) (2023).
8. Zhou, Y., Wexler, A. S. & Wang, L.-P. Modelling turbulent collision of bidisperse inertial particles. *J. Fluid Mech.* **433**, 77–104, DOI: [10.1017/S0022112000003372](https://doi.org/10.1017/S0022112000003372) (2001).
9. Falkovich, G., Fouxon, A. & Stepanov, M. G. Acceleration of rain initiation by cloud turbulence. *Nature* **419**, 151–154, DOI: [10.1038/nature00983](https://doi.org/10.1038/nature00983) (2002).
10. Wilkinson, M. & Mehlig, B. Caustics in turbulent aerosols. *Europhys. Lett. (EPL)* **71**, 186–192, DOI: [10.1209/epl/i2004-10532-7](https://doi.org/10.1209/epl/i2004-10532-7) (2005).
11. Meibohm, J., Sundberg, L., Mehlig, B. & Gustavsson, K. Caustic formation in a non-Gaussian model for turbulent aerosols. *Phys. Rev. Fluids* **9**, 024302, DOI: [10.1103/PhysRevFluids.9.024302](https://doi.org/10.1103/PhysRevFluids.9.024302) (2024).
12. Codispoti, L. A., Meyer, D. W. & Jenny, P. Dissecting inertial clustering and sling dynamics in high-Reynolds number particle-laden turbulence. *Phys. Fluids* **37**, 015161, DOI: [10.1063/5.0244428](https://doi.org/10.1063/5.0244428) (2025).
13. Bewley, G. P., Saw, E.-W. & Bodenschatz, E. Observation of the sling effect. *New J. Phys.* **15**, 083051, DOI: [10.1088/1367-2630/15/8/083051](https://doi.org/10.1088/1367-2630/15/8/083051) (2013).
14. Deepu, P., Ravichandran, S. & Govindarajan, R. Caustics-induced coalescence of small droplets near a vortex. *Phys. Rev. Fluids* **2**, 024305, DOI: [10.1103/PhysRevFluids.2.024305](https://doi.org/10.1103/PhysRevFluids.2.024305) (2017).
15. Fouxon, I., Lee, S. & Lee, C. Intermittency and collisions of fast sedimenting droplets in turbulence. *Phys. Rev. Fluids* **7**, 124303, DOI: [10.1103/PhysRevFluids.7.124303](https://doi.org/10.1103/PhysRevFluids.7.124303) (2022).
16. Ravichandran, S. & Govindarajan, R. Waltz of tiny droplets and the flow they live in. *Phys. Rev. Fluids* **7**, 110512, DOI: [10.1103/PhysRevFluids.7.110512](https://doi.org/10.1103/PhysRevFluids.7.110512) (2022).
17. Siebert, H. *et al.* High-resolution measurement of cloud microphysics and turbulence at a mountaintop station. *Atmospheric Meas. Tech.* **8**, 3219–3228, DOI: [10.5194/amt-8-3219-2015](https://doi.org/10.5194/amt-8-3219-2015) (2015).
18. Feist, M. M. *et al.* Statistics of convective cloud turbulence from a comprehensive turbulence retrieval method for radar observations. *Q. J. Royal Meteorol. Soc.* **145**, 727–744, DOI: [10.1002/qj.3462](https://doi.org/10.1002/qj.3462) (2019).
19. Allwayin, N., Larsen, M. L., Glienke, S. & Shaw, R. A. Locally narrow droplet size distributions are ubiquitous in stratocumulus clouds. *Science* **384**, 528–532, DOI: [10.1126/science.adi5550](https://doi.org/10.1126/science.adi5550) (2024).
20. Thiede, B. *et al.* Highly Localised Droplet Clustering in Shallow Cumulus Clouds, DOI: [10.48550/arXiv.2502.19272](https://doi.org/10.48550/arXiv.2502.19272) (2025). [2502.19272](https://arxiv.org/abs/2502.19272).
21. Shima, S., Kusano, K., Kawano, A., Sugiyama, T. & Kawahara, S. The super-droplet method for the numerical simulation of clouds and precipitation: A particle-based and probabilistic microphysics model coupled with a non-hydrostatic model. *Q. J. Royal Meteorol. Soc.* **135**, 1307–1320, DOI: [10.1002/qj.441](https://doi.org/10.1002/qj.441) (2009).
22. Chandrakar, K. K., Morrison, H., Grabowski, W. W. & Lawson, R. P. Are turbulence effects on droplet collision–coalescence a key to understanding observed rain formation in clouds? *Proc. Natl. Acad. Sci.* **121**, e2319664121, DOI: [10.1073/pnas.2319664121](https://doi.org/10.1073/pnas.2319664121) (2024).
23. Hoffmann, F., Noh, Y. & Raasch, S. The Route to Raindrop Formation in a Shallow Cumulus Cloud Simulated by a Lagrangian Cloud Model. *J. Atmospheric Sci.* **74**, 2125–2142, DOI: [10.1175/JAS-D-16-0220.1](https://doi.org/10.1175/JAS-D-16-0220.1) (2017).
24. Ayala, O., Rosa, B. & Wang, L.-P. Effects of turbulence on the geometric collision rate of sedimenting droplets. Part 2. Theory and parameterization. *New J. Phys.* **10**, 075016, DOI: [10.1088/1367-2630/10/7/075016](https://doi.org/10.1088/1367-2630/10/7/075016) (2008).
25. Maxey, M. R. & Riley, J. J. Equation of motion for a small rigid sphere in a nonuniform flow. *The Phys. Fluids* **26**, 883–889, DOI: [10.1063/1.864230](https://doi.org/10.1063/1.864230) (1983).
26. Sundaram, S. & Collins, L. R. Collision statistics in an isotropic particle-laden turbulent suspension. Part 1. Direct numerical simulations. *J. Fluid Mech.* **335**, 75–109, DOI: [10.1017/S0022112096004454](https://doi.org/10.1017/S0022112096004454) (1997).
27. Gustavsson, K. & Mehlig, B. Statistical models for spatial patterns of heavy particles in turbulence. *Adv. Phys.* **65**, 1–57, DOI: [10.1080/00018732.2016.1164490](https://doi.org/10.1080/00018732.2016.1164490) (2016).

28. Voßkuhle, M., Pumir, A., Lévêque, E. & Wilkinson, M. Prevalence of the sling effect for enhancing collision rates in turbulent suspensions. *J. Fluid Mech.* **749**, 841–852, DOI: [10.1017/jfm.2014.259](https://doi.org/10.1017/jfm.2014.259) (2014).
29. Wilkinson, M., Mehlig, B. & Bezuglyy, V. Caustic Activation of Rain Showers. *Phys. Rev. Lett.* **97**, 048501, DOI: [10.1103/PhysRevLett.97.048501](https://doi.org/10.1103/PhysRevLett.97.048501) (2006).
30. Pan, L. & Padoan, P. Relative velocity of inertial particles in turbulent flows. *J. Fluid Mech.* **661**, 73–107, DOI: [10.1017/S0022112010002855](https://doi.org/10.1017/S0022112010002855) (2010).
31. Abrahamson, J. Collision rates of small particles in a vigorously turbulent fluid. *Chem. Eng. Sci.* **30**, 1371–1379, DOI: [10.1016/0009-2509\(75\)85067-6](https://doi.org/10.1016/0009-2509(75)85067-6) (1975).
32. Ireland, P. J., Bragg, A. D. & Collins, L. R. The effect of Reynolds number on inertial particle dynamics in isotropic turbulence. Part 1. Simulations without gravitational effects. *J. Fluid Mech.* **796**, 617–658, DOI: [10.1017/jfm.2016.238](https://doi.org/10.1017/jfm.2016.238) (2016).
33. Rosa, B., Parishani, H., Ayala, O., Grabowski, W. W. & Wang, L.-P. Kinematic and dynamic collision statistics of cloud droplets from high-resolution simulations. *New J. Phys.* **15**, 045032, DOI: [10.1088/1367-2630/15/4/045032](https://doi.org/10.1088/1367-2630/15/4/045032) (2013).
34. Wang, L.-P., Wexler, A. S. & Zhou, Y. Statistical mechanical description and modelling of turbulent collision of inertial particles. *J. Fluid Mech.* **415**, 117–153, DOI: [10.1017/S0022112000008661](https://doi.org/10.1017/S0022112000008661) (2000).
35. Li, Y. *et al.* A public turbulence database cluster and applications to study Lagrangian evolution of velocity increments in turbulence. *J. Turbul.* **9**, N31, DOI: [10.1080/14685240802376389](https://doi.org/10.1080/14685240802376389) (2008).
36. ETH Zürich. Euler. <https://scicomp.ethz.ch/wiki/Euler>.